Additive Manufacturing 69 (2023) 103532

Contents lists available at ScienceDirect

Additive Manufacturing

journal homepage: www.elsevier.com/locate/addma

Research paper

Modeling and design of three-dimensional voxel printed lattice metamaterials

Le Dong, Jinqiang Wang, Dong Wang [*]

State Key Laboratory of Mechanical System and Vibration, School of Mechanical Engineering, Shanghai Jiao Tong University, Shanghai 200240, China
Meta Robotics Institute, Shanghai Jiao Tong University, Shanghai 200240, China

ARTICLE INFO

Keywords:
3D voxel printing
Lattice metamaterial
Finite deformation model
Tunable mechanical properties

ABSTRACT

3D voxel printing has emerged as a promising technology for fabricating sophisticated structures with voxel-level material distributions, allowing for a wide design space beyond conventional individual material systems. However, the development of theoretical models and design strategies for 3D voxel printed structures are hindered due to the complex geometries and voxel-level material distributions. In this work, we propose a design framework for 3D voxel printed lattice metamaterials by combining theoretical models, finite element modeling (FEM), and experimental validations. We develop a finite deformation theoretical model and propose a python-assisted FEM for the voxel lattice metamaterials with curled microstructures and arbitrary material distributions. We develop a parametric algorithm to generate the voxel matrix for manufacturing automatically. Experiments are conducted to validate the theoretical model and FEM simulations. The design framework is then applied to program mechanical properties by tuning the geometric and material parameters. We demonstrate simultaneous matching of the nonlinear stress–strain and Poisson's ratio curves of biological organisms, shape-matching of porcelain vase and magnetic voxel lattice soft robots with directional locomotion. This work paves the way for designing and manufacturing 3D voxel printed lattice metamaterial with multifunctionality.

1. Introduction

Additive manufacturing (AM) has become a promising technology for fabricating three-dimensional (3D) architectures with sophisticated geometries [1–4]. Besides the geometric design, combining multiple materials in a single structure adds an extra dimension to the design space [5–12], which can be realized by multimaterial additive manufacturing. 3D voxel printing is a representative technology in multimaterial additive manufacturing. Analog to the pixels in 2D images, each voxel is an individually addressable finite-volume element within a 3D object, where the material property and position can be defined independently [13,14]. By rational voxel-by-voxel design in 3D space, the voxelated matters enable tremendous design freedom [15,16] with promising applications in areas such as the conservation and preservation of cultural artifacts [17], learning and education [17] and soft robotics [18,19].

3D voxel printing is similar to the biologically mediated assembly in nature [20–22]. Alike the printing process, cells of animals and plants utilize multiple bio-components (e.g., proteins and polysaccharides) to lay down extracellular matrix (ECM) in a layer-by-layer manner [23,24], which generates variable properties by the distinct arrangement and distribution of the bio-components. For example, the high extensibility of tendons and the anti-cracking property of bones are derived from the integration of spatial structures and protein distribution [25,26]. Tarsal setae, the hairy attachment organs of ladybirds, are endowed with an effective adaptation to rough surfaces due to the graded distribution of elastin and chitin from the tip toward the bases [27]. Such extraordinary functions have inspired the integrated design of structures and material distributions in the engineering field [28–30].

Lattice metamaterials are artificial structures composed of periodically arranged microstructures exhibiting extraordinary properties by rational geometric designs [31–35]. Theoretical models have been developed to guide the design of lattice metamaterials. For instance, Ma et al. studied the nonlinear mechanics of hierarchical lattice materials generated by horseshoe microstructures [36]. The theoretical frameworks were further developed for lattice metamaterials with diverse geometrics, such as serpentine [37], rotatable [38], and fractal [39]. However, the above work mainly focused on the geometric design and neglected the effects of material distributions, which cannot fully exploit the potentials of lattice metamaterials.

---

[*] Correspondence to: School of Mechanical Engineering, Shanghai Jiao Tong University, Shanghai 200240, China.
E-mail address: wang_dong@sjtu.edu.cn (D. Wang).

https://doi.org/10.1016/j.addma.2023.103532
Received 19 November 2022; Received in revised form 21 March 2023; Accepted 27 March 2023

The development of AM technologies has spawned studies on multimaterial lattice metamaterials [40–45]. For example, Ge et al. reported highly stretchable multimaterial hydrogel composites with drug-releasing functions [46]. Mirzaali et al. developed multimaterial cellular metamaterial with tunable elastic properties [47]. Recently, machine learning and evolutionary algorithm have been efficiently utilized to enable the customizable mechanical behaviors of lattice metamaterials. For example, Deng et al. developed a design workflow for hinged quadrilateral lattice metamaterials with target nonlinear response via a neural accelerated evolution strategy [48]. Zeng et al. proposed a topology optimization for energy-absorbing lattice metamaterials based on genetic algorithm [49]. Hamel et al. introduced a machine learning based approach for the deformation control of 4D printed active composite structures [50]. By 3D voxel printing, lattice metamaterials with voxel-level material distributions can be achieved, exhibiting diverse functions and further expanding the application prospects. The ability to distribute multiple materials precisely increases the structures' design freedom but simultaneously imposes emerging challenges on the modeling and design. Our previous work developed a combined machine learning and evolutionary algorithm based on FEM data to optimal design voxel printed lattice metamaterials [51]. However, the lack of theoretical models hinders understanding the underlying physics and more efficient and diverse designs. Therefore, developing theoretical modeling of voxel printed lattice metamaterials that considers the voxel-level material distribution, complex geometry, and finite deformation is highly needed.

In this work, we develop a design framework for 3D voxel printed lattice materials by integrating the parametric generation of the voxel matrix, finite deformation theoretical model, python-assisted FEM, and experimental validation. As depicted in Fig. 1, the voxel matrix is generated first, including the geometric design and material distribution information. Secondly, a previously developed theoretical model for the lattice metamaterials is extended to account for the voxel-level material distribution, complex geometry, and finite deformation. Python-assisted FEM simulations for lattice metamaterials with voxel material distributions are conducted. Thirdly, 3D voxel printing is applied to fabricate the lattice metamaterials (Fig. 1(b) and (c)), which are used to validate the theoretical model and FEM simulations. The combined theoretical, FEM, and experimental framework is then used to design the mechanical properties by tuning the geometric and material parameters. We demonstrate simultaneous matching of the nonlinear stress–strain and Poisson's ratio curves of biological organisms, shape-matching of porcelain vases, magnetic voxel lattice soft robots and voxel soft grippers using the developed design framework (Fig. 1(d)).

2. Structural geometry and material characterization

2.1. Geometry and material design

Fig. 1(a) shows the geometric and material design of the lattice metamaterials. The geometry was formed by replacing straight beams in a lattice pattern with antisymmetric microstructures. Three typical unit patterns were used: triangular, rectangular, and hexagonal patterns. The microstructures can be constructed using parametric functions in Cartesian coordinates or curvature functions in polar coordinates. The curvature functions defined the relationship between the slope angle α and the instantaneous radius of curvature R. The microstructures were antisymmetric with respect to the origin. The periodic unit of the lattice metamaterials can be constructed by different microstructures.

3D voxel printing allows accurate material distributions on the micrometer scale. Different from the conventional single-material design, hard (cyan color) and soft (red color) materials were used. The volume fraction of the hard material V_f was used to characterize the material distribution. By mixing the hard and soft materials on a voxel scale, various moduli in between can be formed. In particular, functional gradient structures can be formed by varying V_f continuously. The voxel matrix of the lattice metamaterial containing the geometric and material information was generated for 3D voxel printing. A home-written MATLAB script was used to automatically perform the process, which consisted of the following three steps. (i) The 2D sketch of each microstructure was formed by constructing the central curve using parametric functions first and then offset to add width information. The 2D sketch was then converted to a binary voxel matrix, in which 1 represented solid and 0 represented void. (ii) Material information was then added into the voxel matrix by modifying the binary values depending on the material distributions. Each value represented a specific material. (iii) The voxel matrix of the lattice metamaterial was then formed by transforming and merging the voxel matrix of microstructures.

Analog to the pixels in 2D images, each voxel is an individually addressable finite-volume element within a 3D object. Voxels can be stored as a virtual three-dimensional matrix, the individual elements defining the material property and position. 3D voxel printing enables accurate material distributions layer by layer. Fig. S3 shows the voxel matrix of lattice metamaterial in one layer. Each voxel in the matrix has a corresponding position coordinate representing the geometric information. The specific value of the voxel indicates the material information, where 0 represents no material, 1 represents soft material and 2 represents hard material.

2.2. Material characterization and fabrication

The lattice metamaterials were fabricated using a material jetting additive manufacturing system J750 (Fig. 1(b) and (c)). Each voxel in the voxel matrix defined the material and 3D placement of a jetting droplet. The dimension of each voxel was 42 μm × 8 μm × 27 μm. Verowhite (Stratasys, MN, USA) and Agilus (Stratasys, MN, USA) were chosen as the hard and soft digital materials. Young's moduli of Verowhite and Agilus were 1.5 GPa and 0.5 MPa, respectively. The Poisson's ratios $\nu = 0.3$. Young's modulus (E) can be tuned over three orders of magnitude (from 0.5 MPa to 1.5 GPa) by varying V_f. Tensile tests were conducted to test Young's modulus of dog-bone tensile specimens with different V_f. A uniaxial materials testing system (Instron 68SC-2) was used with a tensile rate of 5 mm/min. The experimental stress–strain curves are shown in Fig. S1(a). The Young's moduli with various V_f were obtained by linearly fitting the curves with a 5% strain. The relationship between Young's modulus and V_f is shown in Fig. S1(b).

2.3. Python-assisted FEM model

We developed a Python-assisted FEM model to perform numerical analysis by resolving the difficulties resulting from the complex geometries and voxel-level material distributions. The FEM was carried out using the commercial software ABAQUS (SIMULIA, Providence, RI). The Python script allowed for assigning the materials on each element. The node and element information were extracted and the Young's modulus was assigned according to the voxel matrix using the Python script. Geometric information can also be programmed, such as the cross-section properties. 3-node quadratic hybrid beam elements (B32H) were used. Refined meshes were adopted to ensure computational accuracy. The lower boundary of the lattice metamaterial was fixed and a vertical displacement was applied to the upper boundary. Quasi-static simulations were performed using Abaqus/Standard.

3. Modeling of 3D voxel printed lattice metamaterials

In this section, the previously developed theoretical model for lattice metamaterials was extended to incorporate the multimaterial distributions and varying microstructures.

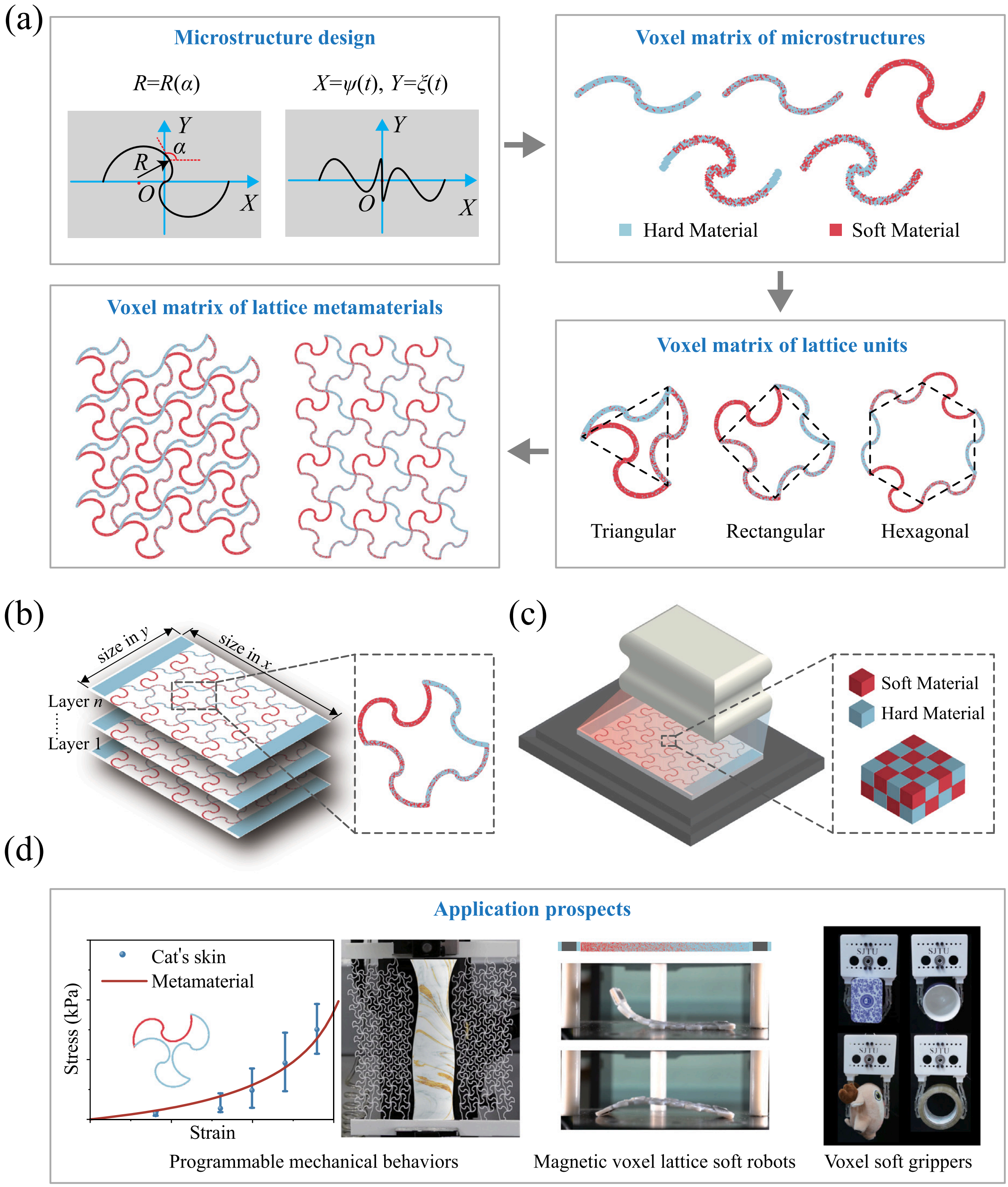

Fig. 1. The design framework of 3D voxel printed lattice metamaterials. The design procedures include (a) geometric design, generation of the voxel matrices of microstructures, lattice units, and lattice metamaterials. (b) Voxel slices of lattice metamaterials. (c) Manufacturing process using 3D voxel printing. (d) Application prospects including programmable mechanical behaviors, magnetic voxel lattice soft robots and voxel soft grippers. (For interpretation of the references to color in this figure legend, the reader is referred to the web version of this article.)

3.1. Theoretical model of voxel microstructure

Consider a 3D voxel printed lattice metamaterial under uniaxial stretching, as depicted in Fig. 2. The geometry of microstructure was generated by $R(\alpha)$, $\alpha_0 \leq \alpha \leq \alpha_{end}$, where α_0 and α_{end} are the initial and end slope angle of the designed microstructure. The material distribution was characterized by $V_f(\alpha)$. The Young's modulus of microstructure was therefore defined as $E(\alpha) = E(V_f(\alpha))$. The voxel microstructure was modeled as a simple supported with the horizontal force F_x, vertical force F_y, and moment F_0 at both ends. The coordinates of each point on the half of the undeformed microstructure can be obtained as

$$\begin{pmatrix} X(\alpha) \\ Y(\alpha) \end{pmatrix} = \int_{\alpha_0}^{\alpha} R(\alpha) \begin{pmatrix} \cos\alpha \\ \sin\alpha \end{pmatrix} d\alpha. \tag{1}$$

Due to the antisymmetric geometry and material distribution, each microstructure has an antisymmetrical deformation when uniaxial stretched. Only half of the voxel microstructure is needed to be analyzed (Fig. 2(a)). For an infinitesimal segment of voxel microstructure in the X–Y plane, the tangent angle α and length dS in the initial

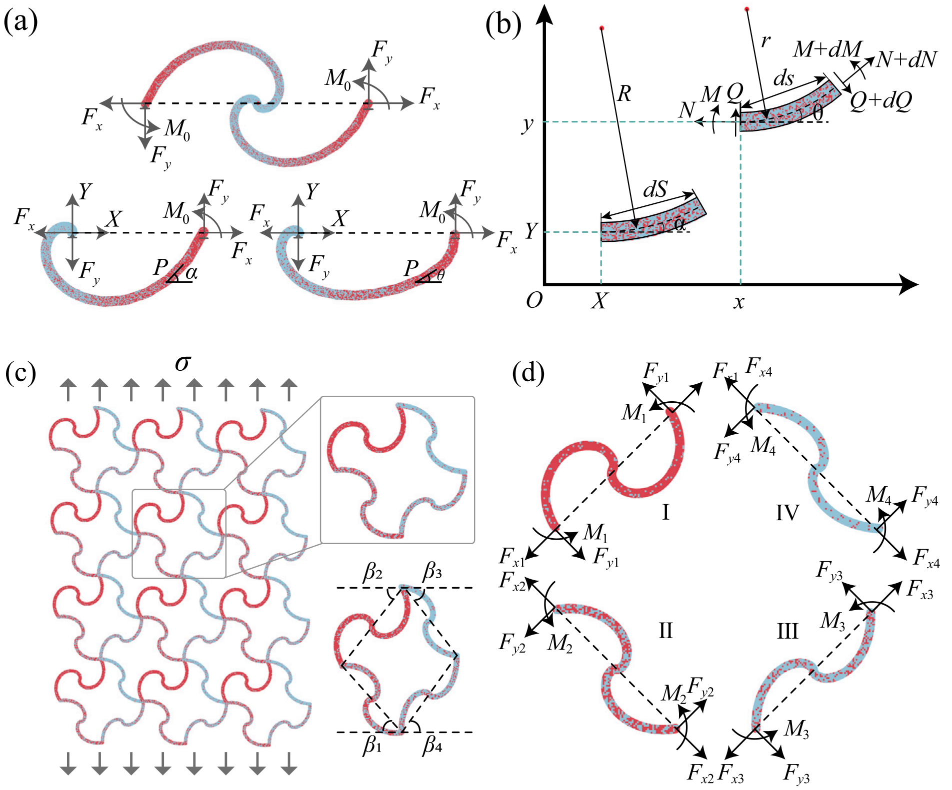

Fig. 2. Theoretical model for 3D voxel printed lattice metamaterials. (a) The microstructure is simply supported with the horizontal force F_x, vertical force F_y, and moment M_0 at both ends. The slope angle at a point P deforms from α to θ. (b) The inner forces and moments of an infinitesimal beam element before and after deformation. (c) A rectangular lattice metamaterial with four different microstructures under uniaxial vertical stress σ. The undeformed and deformed shapes of a representative unit are shown. (d) Inner forces and moments on each microstructure.

state became θ and ds after deformation. The rotational angle and the strain at the centroid axis were given by $\varphi = \theta - \alpha$ and $\varepsilon = (ds - dS)/ds$, where $ds = r(\theta)d\theta, dS = R(\alpha)d\alpha$. $R(\alpha)$ and $r(\theta)$ were the radii of the microstructure in undeformed and deformed configurations, respectively. We denoted the axial force, shear force and bending moment as N, Q and M on the cross-section.

For a linear elastic material with Young's modulus $E(\alpha)$, N and M are given by

$$N = E(\alpha)A\varepsilon \text{ and } M = E(\alpha)I\frac{d\varphi}{dS}, \tag{2}$$

where A and I represent the area and moment of inertia of the cross-section. According to the static equilibrium, we can get

$$N = F_x\cos\theta + F_y\sin\theta \text{ and } Q = F_x\sin\theta - F_y\cos\theta. \tag{3}$$

The equilibrium equations can be written in terms of the internal forces and moments as

$$\frac{dN}{ds} + \frac{Q}{r} = 0, -\frac{N}{r} + \frac{dQ}{ds} = 0, \text{ and } \frac{dM}{ds} = Q. \tag{4}$$

Substitution of Eqs. (2) and (3) into Eq. (4) gives

$$\frac{d^2\varphi}{dS^2} = \frac{\left(E(\alpha)A + F_x\cos\theta + F_y\sin\theta\right)\cdot\left(F_x\sin\theta - F_y\cos\theta\right)}{E(\alpha)I\cdot E(\alpha)A}. \tag{5}$$

Using $dS = R(\alpha)d\alpha$, $\frac{d\varphi}{d\alpha} = \frac{d\theta}{d\alpha} - 1$ and $\frac{d^2\varphi}{d\alpha^2} = \frac{d^2\theta}{d\alpha^2}$, Eq. (5) becomes

$$\begin{aligned}\frac{d^2\theta}{d\alpha^2} &= -R\frac{d(R^{-1})}{d\alpha}(\frac{d\theta}{d\alpha} - 1)\\ &+ \frac{R^2\left(E(\alpha)A + F_x\cos\theta + F_y\sin\theta\right)\left(F_x\sin\theta - F_y\cos\theta\right)}{E(\alpha)I\cdot E(\alpha)A},\end{aligned} \tag{6}$$

with the following two boundary conditions

$$\frac{d\theta}{d\alpha}(\alpha = \alpha_0) = 1, \tag{7}$$

$$l_y = \int_{\alpha_0}^{\alpha_{end}} (1+\varepsilon)R(\alpha)\sin\theta d\alpha = 0. \tag{8}$$

The first boundary condition (Eq. (7)) implies a null moment at the center point of a microstructure. When a voxel lattice structure is subjected to a uniaxial stretching, each microstructure undergoes anti-symmetric deformation relative to the central point due to its anti-symmetrical design. With no additional moment applied at the center, the moment at the center remains null. The second boundary conditions (Eq. (8)) means the ends and the center point of the deformed microstructure are on the same horizontal alignment due to the anti-symmetric geometry. l_y represents the distance between the ends and the center point of the microstructure along the y-axis.

The voxelized material distribution was defined on the undeformed configuration. As shown in Fig. 2(a), a point P moves during deformation and its slope angles before and after deformation change from α to θ. The relation between α and θ was not prescribed. It was obtained by solving the second-order ordinary differential Eq. (6) with two boundary conditions Eqs. (7) and (8). The deformed shape of the voxel microstructure can be obtained. The coordinates of the right half are given by

$$\begin{pmatrix} x(\theta) \\ y(\theta) \end{pmatrix} = \int_{\theta_0}^{\theta} (1+\varepsilon)R(\theta)\begin{pmatrix} \cos\theta \\ \sin\theta \end{pmatrix} d\theta, \tag{9}$$

where $\theta_0 \le \theta \le \theta_{end}$. θ_0 and θ_{end} are corresponding to α_0 and α_{end} at the deformed configuration. The mechanism of voxel microstructures generated by the parametric function $X = \psi(t)$ and $Y = \zeta(t)$ was also studied. Details are given in the Supporting Information S1.

3.2. Theoretical model of 3D voxel printed lattice metamaterials with distinct microstructures

We investigated the deformation of rectangular 3D voxel printed lattice metamaterials under transverse vertical load σ_{xx}, longitudinal vertical load σ_{yy}, and shear load $\sigma_{xy}(\sigma_{xy} = \sigma_{yx})$. As shown in Fig. 2(d), each representative unit cell consists of four microstructures indexed from I to IV. The static equilibrium of the unit cell gives the relations between the inner forces and the external loading. In the normal and shear directions, it requires that

$$\begin{pmatrix} \cos\beta_2 & -\sin\beta_2 & \cos\beta_1 & \cos\beta_2 & 0 & 0 & 0 & 0 \\ \sin\beta_2 & \cos\beta_2 & 0 & 0 & 0 & 0 & \sin\beta_3 & -\cos\beta_3 \\ -\sin\beta_2 & -\cos\beta_2 & \sin\beta_1 & -\cos\beta_1 & 0 & 0 & 0 & 0 \\ 0 & 0 & 0 & 0 & -\sin\beta_4 & -\cos\beta_4 & \sin\beta_3 & \cos\beta_3 \\ -\cos\beta_2 & \sin\beta_2 & 0 & 0 & 0 & 0 & \cos\beta_3 & \sin\beta_3 \\ 0 & 0 & \cos\beta_1 & \sin\beta_1 & -\cos\beta_4 & \sin\beta_4 & 0 & 0 \end{pmatrix}$$

$$\times \begin{pmatrix} F_{x1} \\ F_{y1} \\ F_{x2} \\ F_{y2} \\ F_{x3} \\ F_{y3} \\ F_{x4} \\ F_{y4} \end{pmatrix} = \begin{pmatrix} \sqrt{2}Ld\sigma_{xx} \\ \sqrt{2}Ld\sigma_{yy} \\ \sqrt{2}Ld\sigma_{yx} \\ \sqrt{2}Ld\sigma_{yx} \\ \sqrt{2}Ld\sigma_{xy} \\ \sqrt{2}Ld\sigma_{xy} \end{pmatrix}. \tag{10}$$

The moment equilibrium of an arbitrary joint, which is connected by four microstructures, and the anti-symmetry requires that

$$\sum_{i=1}^{4} M_i = -\sum_{i=1}^{4} (F_{yi} L_i)/2 = 0, \tag{11}$$

where L is the initial horizontal length of the microstructures. L_i is the deformed horizontal length of the corresponding microstructures.

The angle between the tangent directions of two connected microstructures remains unchanged during deformation. It gives

$$\begin{pmatrix} 0 & 1 & 1 & 0 \\ 1 & 0 & 0 & 1 \\ 1 & 1 & 0 & 0 \end{pmatrix} \begin{pmatrix} \beta_1 \\ \beta_2 \\ \beta_3 \\ \beta_4 \end{pmatrix} + \begin{pmatrix} 1 & 0 & 0 & -1 \\ 0 & -1 & 1 & 0 \\ 1 & -1 & 0 & 0 \end{pmatrix} \begin{pmatrix} \theta_1 \\ \theta_2 \\ \theta_3 \\ \theta_4 \end{pmatrix} = \begin{pmatrix} \frac{\pi}{2} \\ \frac{\pi}{2} \\ \frac{\pi}{2} \end{pmatrix}. \tag{12}$$

The deformation compatibility requires that the side lengths and interior angles of the deformed rectangle should satisfy the following geometric relations

$$\begin{pmatrix} \sin\beta_2 & \sin\beta_1 & -\sin\beta_4 & -\sin\beta_3 \\ \cos\beta_2 & -\cos\beta_1 & -\cos\beta_4 & \cos\beta_3 \end{pmatrix} \begin{pmatrix} L_1 \\ L_2 \\ L_3 \\ L_4 \end{pmatrix} = 0. \tag{13}$$

The deformed configurations of 3D voxel printed lattice metamaterials can be obtained by solving Eqs. (10)–(13) and the governing equations of the voxel microstructures Eqs. (6)–(8). The longitudinal strain ε_y and Poisson's ratio ν can be written as

$$\varepsilon_y = \frac{L_1 \sin\beta_2 + L_2 \sin\beta_1 - \sqrt{2}L}{\sqrt{2}L}, \tag{14}$$

$$\nu = -\frac{L_3 \cos\beta_4 + L_4 \cos\beta_2 - \sqrt{2}L}{L_1 \sin\beta_2 + L_2 \sin\beta_1 - \sqrt{2}\widehat{L}}. \tag{15}$$

The theoretical models of triangular and hexagonal 3D voxel printed lattice metamaterial can be derived similarly. The details are shown in the Supporting Information S2.

4. Validation of the theoretical model

Experiments and FEM simulations were conducted to validate the theoretical model. Here three lattice metamaterials were designed and tested. The first lattice metamaterial consisted of distinct microstructures fabricated from the same material, while the second lattice metamaterial was composed of microstructures with the same geometry but different material distributions. Two different gradient material distributions were used for the microstructures of the third lattice metamaterials.

4.1. Lattice metamaterials with distinct microstructures

The first lattice metamaterial included 5 × 8 units constructed by four different microstructures (Fig. 3(a)). The curvature functions of microstructures I to IV were $R(\alpha) = \alpha$ $(0 \le \alpha \le 4.5)$, $R(\alpha) = \alpha^2$ $(0 \le \alpha \le 4.1)$, $R(\alpha) = \alpha^{2.5}$ $(0 \le \alpha \le 4.0)$, and $R(\alpha) = \alpha^3$ $(0 \le \alpha \le 3.9)$, respectively. All the microstructures were scaled to $L = 10\sqrt{2}$mm. The cross-sectional width $w = 0.2$ mm and the thickness $d = 3$ mm. The same material with $E = 1.5$ GPa was used. Experiments and FEM simulations of tension tests were conducted to compare with the theoretical model. The experimental, FEM, and theoretical J-shaped tensile curves and deformed unit shapes agreed well (Fig. 3(d) and Video. S1). The J-shaped stress–strain curves result from the transitions from bending-dominant to stretch-dominant deformation. Besides the rectangular patterns, triangular and hexagonal lattice metamaterial were also tested and compared with the theoretical and FEM simulated results in Fig. S4. Due to the initial structural uncurling, the hexagonal lattice metamaterials showed a slower increase in the tangent modulus with the increased applied strain than triangular and rectangular metamaterials. For instance, the axial strain of triangular, rectangular, and hexagonal lattice metamaterials was around 32%, 75%, and 100% under $\sigma_{yy} = 200$ kPa, respectively.

The mechanical behaviors of lattice metamaterials with varying cross-sections can also be studied using the developed model. Unlike previous work where the cross-section was generally constant or piecewise constant, Fig. S7 shows a lattice metamaterial whose cross-section varies continuously with α. The cross-section was designed by $A(\alpha) = w(\alpha) * d$, where $w = (0.2+0.08\alpha)$ mm and $d = 3$ mm. $V_f = 0.87$ ($E = 1.2$ GPa). By replacing A and I in Eq. (6) as $A(\alpha)$ and $I(\alpha)$, the theoretical solutions can be calculated and compared with the experiments and FEM. The theoretical results agreed well with the FEM simulations but slightly differ from the experiments, which may be due to the structural defects caused by voxel printing.

4.2. Lattice metamaterials with multimaterial distributions

Fig. 3(b) shows the second lattice metamaterial consisting of three microstructures with different V_f (0.94, 0.7, and 0.5). The corresponding Young's moduli were 1.4 GPa, 800 MPa, and 200 MPa. All the microstructures were built using the same radius function $R(\alpha) = \alpha$ $(0 \le \alpha \le 4.5)$. $w = 0.3$ mm and $d = 2$ mm. The experimental, FEM, and theoretical tensile stress–strain curves and deformed shapes agreed well (Fig. 3(e) and Video. S1). For comparison, a homogeneous triangular lattice metamaterial was designed with the same overall material composition ($V_f = 0.72$, $E = 820$ MPa) in Fig. S5. We can observe that the J-shaped stress–strain curves and Poisson's ratio of triangular lattice metamaterials can be tuned by varying the material distribution. For example, the tensile stress increased from 9.5 kPa (homogeneous metamaterial) to 11 kPa (metamaterial with multimaterial distribution) when $\varepsilon = 40\%$, while the Poisson's ratio changed from a negative (−0.18) to a positive value (0.06).

Fig. 3(c) shows the third lattice metamaterials consisting of four microstructures with two types of gradient material distributions. For microstructures I and III, Young's modulus was set as $E(\alpha) = 50 + 1450\alpha/\alpha_{end}$, $(0 \le \alpha \le 7.4)$ with $\alpha_{end} = 7.4$. The modulus of the

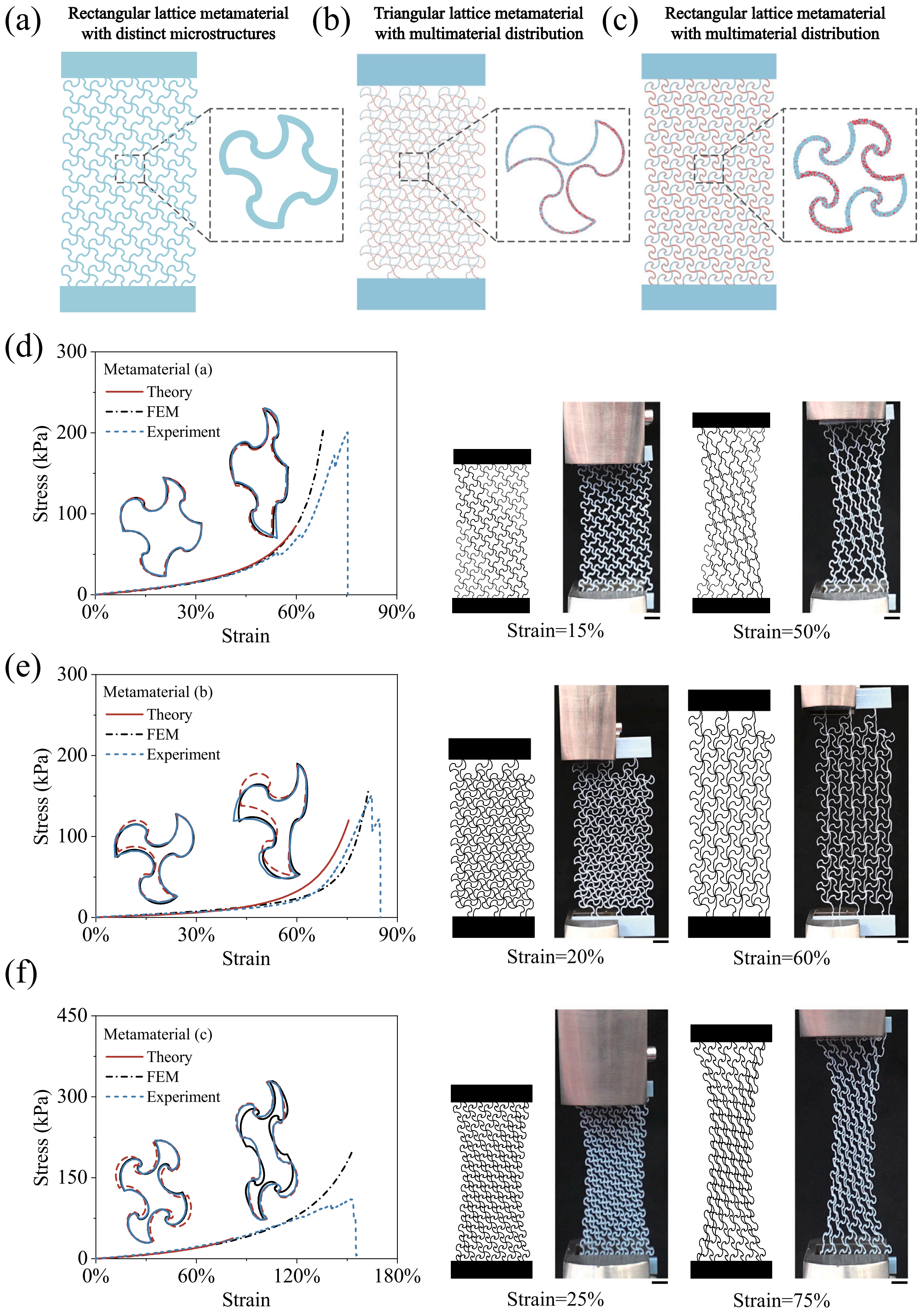

Fig. 3. Validation of the theoretical model. Voxel slices of (a) a rectangular lattice with distinct microstructures, (b) a triangular and (c) a rectangular lattice metamaterial with multimaterial distribution. (d), (e) and (f) show the experimental, theoretical and FEM uniaxial tensile curves of lattice metamaterials (a), (b), (c), respectively. Insets show the theoretical, experimental, and FEM deformed shapes of the representative units. The optical image and FEM simulations of the tension test at specified strains. All scale bars are 10 mm.

microstructure increased from 50 MPa to 1.5 GPa as α increased. For microstructures II and IV, $E(\alpha) = 1500 - 1450\alpha/\alpha_{end}$. The modulus of microstructures II and IV decreased from 1.5 GPa to 50 MPa as α increased. The geometries of the microstructures were the same and designed by $R(\alpha) = \alpha^3 + \alpha^2 + \alpha - 1$ ($0 \le \alpha \le 7.4$). Similarly, a homogeneous rectangular lattice metamaterial was built with the same overall material composition ($V_f = 0.71$, $E = 806$ MPa). The theoretical, experimental, and FEM simulated results agreed well for both lattice metamaterials, (Fig. 3(f), Fig. S6, and Video S1). The use of gradient material distribution led to a significant change in the mechanical behaviors. For instance, the stress decreased from 40 kPa to 29 kPa and the corresponding Poisson's ratio increased from 0.36 to 0.65 at $\varepsilon = 75\%$, when the material distribution changed from homogeneous to gradient.

5. Applications

The theoretical model can further guide multifunctional applications. The effects of material and geometric parameters of lattice metamaterials were investigated. Bionic stress–strain matching, shape-matching lattice metamaterials, and magnetic voxel lattice soft robots were demonstrated.

5.1. Programmable Poisson's ratio

The effects of material and geometric parameters of the three microstructures on Poisson's effect of a triangular lattice metamaterial were studied. By designing the material compositions of the microstructures I-III separately, the 3D voxel printed triangular lattice metamaterial exhibited a tunable Poisson's ratio from negative to positive. We constructed a series of triangular lattice metamaterials by adjusting Young's modulus of each microstructure within the range [100MPa, 1.5 GPa]. The geometries of the microstructures were the same as those used in Fig. 3(b). Fig. 4(a) shows the design space of the Poisson's ratio for three different E_{III} = 100 MPa, 660 MPa, and 1500 MPa at an applied strain $\varepsilon = 45\%$. Similar trends can be observed. When the material choice changed from the left-top to the right-bottom corner, the Poisson's ratio gradually changed from a large positive value to zero or even negative. For example, the Poisson's ratio changed from 0.25 to −0.16 as E_{I} = 100 MPa and E_{II} = 1500 MPa changed to E_{II} = 100 MPa and E_{I} = 100 MPa with a fixed E_{III} = 660 MPa. We can also observe that the Poisson's ratio decreased from positive to negative as E_{III} increased. Three typical lattice metamaterials with positive, nearly zero or negative Poisson's ratios were chosen from the design space maps (marked by stars). The corresponding voxel slices and periodic units are shown in Fig. 4(b)–(d). The FEM simulated and theoretical deformed shapes are shown in Fig. 4(e)–(g).

Fig. 4(h) shows that the Poisson's ratio can also be tuned by varying the geometry of the microstructures. The curvature function $R(\alpha) = \alpha^n (1 \le n \le 3)$ was used to generate various microstructures by varying n. The periodic unit of each triangular lattice metamaterial consisted of three microstructures with different n. The design space maps of Poisson's ratio by varying the n for microstructure I (n_{I}) and II (n_{II}) at different n for microstructure III (n_{III} = 1, 2, and 3) were shown. The maps showed that the Poisson's ratio ranges from −0.2 to 0.8 by tuning n.

5.2. Stress–strain matching and shape-matching designs

The programmable mechanical responses of 3D voxel printed lattice metamaterial with distinct microstructures allowed for multifunctional designs. Here stress–strain matching and shape-matching lattice metamaterials were designed. Many biological tissues exhibit J-shaped stress–strain curves and nonlinear Poisson's ratio. The metamaterial reproducing the bionic mechanical behaviors holds promise in bio-integrated devices to avoid discomfort induced by the mechanical mismatch. As shown in Fig. 5(a) and (b), the rationally designed triangular metamaterial can simultaneously mimic the J-shaped stress–strain curves and negative Poisson's ratio of the cat's skin. The design functions of the microstructure I-III were $R(\alpha) = \alpha^n$, where $n_{\mathrm{I}} = 1.1$ and $n_{\mathrm{II}} = n_{\mathrm{III}} = 1$, respectively. The corresponding material parameter $E_{\mathrm{I}} = E_{\mathrm{III}}$ = 1500 MPa and E_{II} = 0.5 MPa.

Fig. 5(c) demonstrates a shape-matching design, realized by combining triangular lattice metamaterials with different Poisson's ratio. Three subregions were used. Subregions i-iii corresponded to negative Poisson's ratio, positive Poisson's ratio and nearly zero Poisson's ratio regions, respectively. The design parameters and periodic units are illustrated in Fig. 5(d). The optical image of the 3D voxel printed lattice metamaterials at $\varepsilon = 45\%$ is shown in Fig. 5(f). The lateral profiles of a porcelain vase can be accurately reproduced. FEM simulations were conducted for comparison and display well agreements (Fig. 5(e) and Video. S2).

5.3. Magnetic voxel lattice soft robot

Lattice metamaterials have shown promising applications in soft robotics, whose motion was mainly controlled by the embedded intelligence in the structures and materials. 3D voxel printing provides a way to program movement through structural and material designs. We demonstrated a magnetic voxel lattice soft robot with controllable motions. The lattice soft robot consisted of a 3D voxel printed lattice metamaterial and two magnetic cells with opposite magnetization directions (Fig. 6(a)). The lattice design enabled lightweight (~2 g) and large deformation, facilitating fast and dexterous locomotion. Rectangular lattice metamaterials with three material distributions were designed: homogenized, biaxial-graded, and lateral-graded material distributions. The magnetic cells were magnetized in the Z direction. Fabrication details are given in the Supporting Information.

Two types of magnetic fields were applied: (i) a sinusoidal magnetic field B_X in the X direction and a uniform magnetic field B_Z in the Z direction (Fig. 6(b)); (ii) a sinusoidal magnetic field B_X in the X direction (Fig. 6(g)). In the presence of an external magnetic field B, a magnetic torque $M = N \times B$ was generated, which tended to align the magnetization direction N with the magnetic field direction B.

In case (i), the lattice soft robot with homogenized material (E = 810MPa) showed a crawling motion toward the X direction with a speed of 1.6 mm/s. Under magnetic fields B_X and B_Z, the left side of the lattice soft robot bent higher, as the additional magnetic field B_Z along the Z direction was applied to break the symmetry. Therefore, large elastic energy was stored in the left part. When B_X reverses, the elastic energy was released, and the lattice soft robot formed an inward asymmetric bending shape. The peak of the asymmetric bending shape was located at the left side. The asymmetric bending shape caused different contact with the substrate, which led to differential locomotion towards the right direction. Details are given in the Supporting Information S5. The lateral-graded material distribution further enhanced the asymmetry. The bending stiffness was relatively lower than the right side due to uneven material distributions, leading to a locomotion speed of 4.7 mm/s, around 3 times the homogenized lattice soft robots (Fig. S11 and Video. S3).

We developed an analytical model to guide the design of the crawling motion of the magnetic soft robot with lateral-graded material distribution. The lattice structures showed an out-of-plane bending under a magnetic field. As the geometry and the material distribution were complex, we simplified the lattice metamaterial to a beam with effective modulus distribution.

The theoretical predicted stress–strain curves of lattice metamaterials with uniform volume fraction V_f = 0 to 1 are shown in Fig. 6(c). The effective modulus was obtained by linearly fitting the curves with a 50% strain. The relationship between the effective moduli and the volume fraction was obtained (Fig. 6(d)). The beam model was then used to estimate the deformation of the magnetic soft robot under a magnetic field Fig. 6(e). In case (1), the lattice in stage II (Fig. 6(f)) was modeled as a cantilever beam with its right end clamped and left end under a moment M. The moment acting at any point (x, y) was also M. Using the Euler–Bernoulli moment–curvature relationship

$$\frac{\mathrm{d}\delta}{\mathrm{d}s} = \frac{M}{E(s)I}, \tag{16}$$

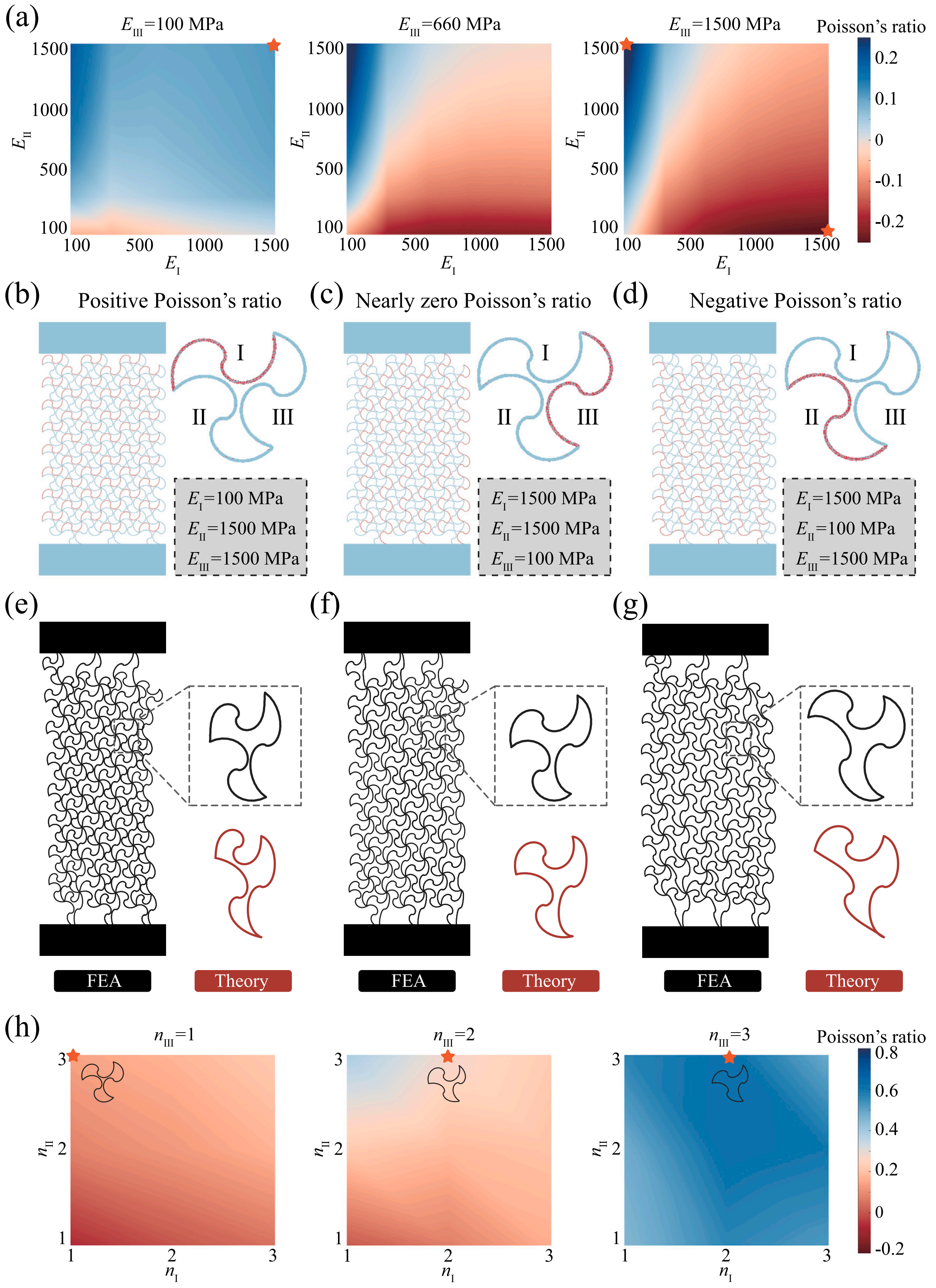

Fig. 4. Programmable mechanical behaviors. (a) Tunable Poisson's ratio at $\varepsilon = 45\%$ enabled by adjusting Young's modulus of microstructure I-III within the range [100 MPa, 1.5 GPa] individually. Three typical 3D voxel printed triangular lattice metamaterials with (b) negative, (c) nearly zero and (d) positive Poisson's ratio. (e), (f) and (g) show the FEM deformed shapes of the lattice metamaterials, and the theoretical and FEM deformed representative units. (h) Tunable Poisson's ratio at $\varepsilon = 40\%$ enabled by individually adjusting the geometric parameters n of microstructure I-III within the range [1, 3].

where δ is the slope angle at point (x, y). s is the distance along the beam from that point to the fixed end. $E(s)$ is the effective modulus corresponding to the designed voxel distribution. $E(s)I$ is the flexural rigidity of the beam. M is the applied bending moment. The cantilever is subjected to the following boundary condition

$$\delta|_{s=0} = 0. \tag{17}$$

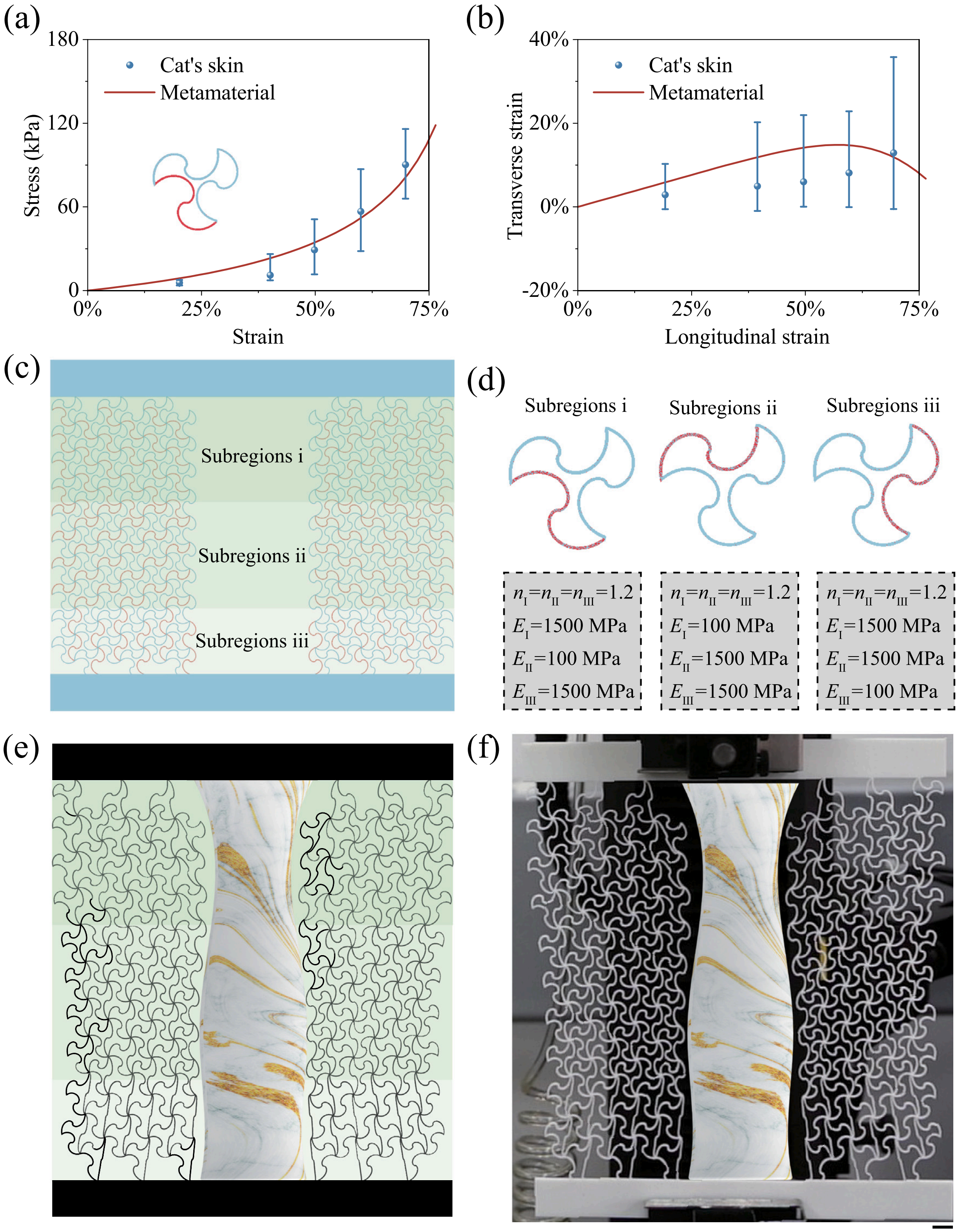

Fig. 5. Multifunctional designs. Simultaneous reproduction of (a) the J-shaped stress–strain curves and (b) negative Poisson's ratio of cat's skin by a 3D voxel printed triangular lattice metamaterial. (c) shows a subregional design for matching the lateral profile of a porcelain vase. (d) Design parameters and voxel units of each subregion. (e) and (f) show the experimental and FEM simulation of the 3D voxel printed lattice metamaterials at $\varepsilon = 45\%$. The scale bar is 10 mm.
Source: Data from Ref. [52].

The applied moment M should satisfy

$$M = NB\sin(\varphi) \text{ with } \varphi = 3\pi/4 - \delta_{end}, \tag{18}$$

where N is the magnetization of the magnetic cell and the measured value is 123 kA/m (Fig. S9). B represents the synthetic magnetic field strength with an amplitude of 14.14 mT. δ is the angle between the direction of N and B, which is related to the slope angle at the end of the beam (δ_{end}) as shown in Fig. 6(e).

By solving Eq. (16) with boundary condition Eq. (17) and load requirement Eq. (18), δ can be obtained, and the deformed shape of the beam can be further generated by numerically integrating δ. In case (2), The deformed configuration in stage IV was modeled as a simply supported beam. The boundary condition at the free end with no longitudinal displacement is

$$\int_0^s \sin\delta ds = 0. \tag{19}$$

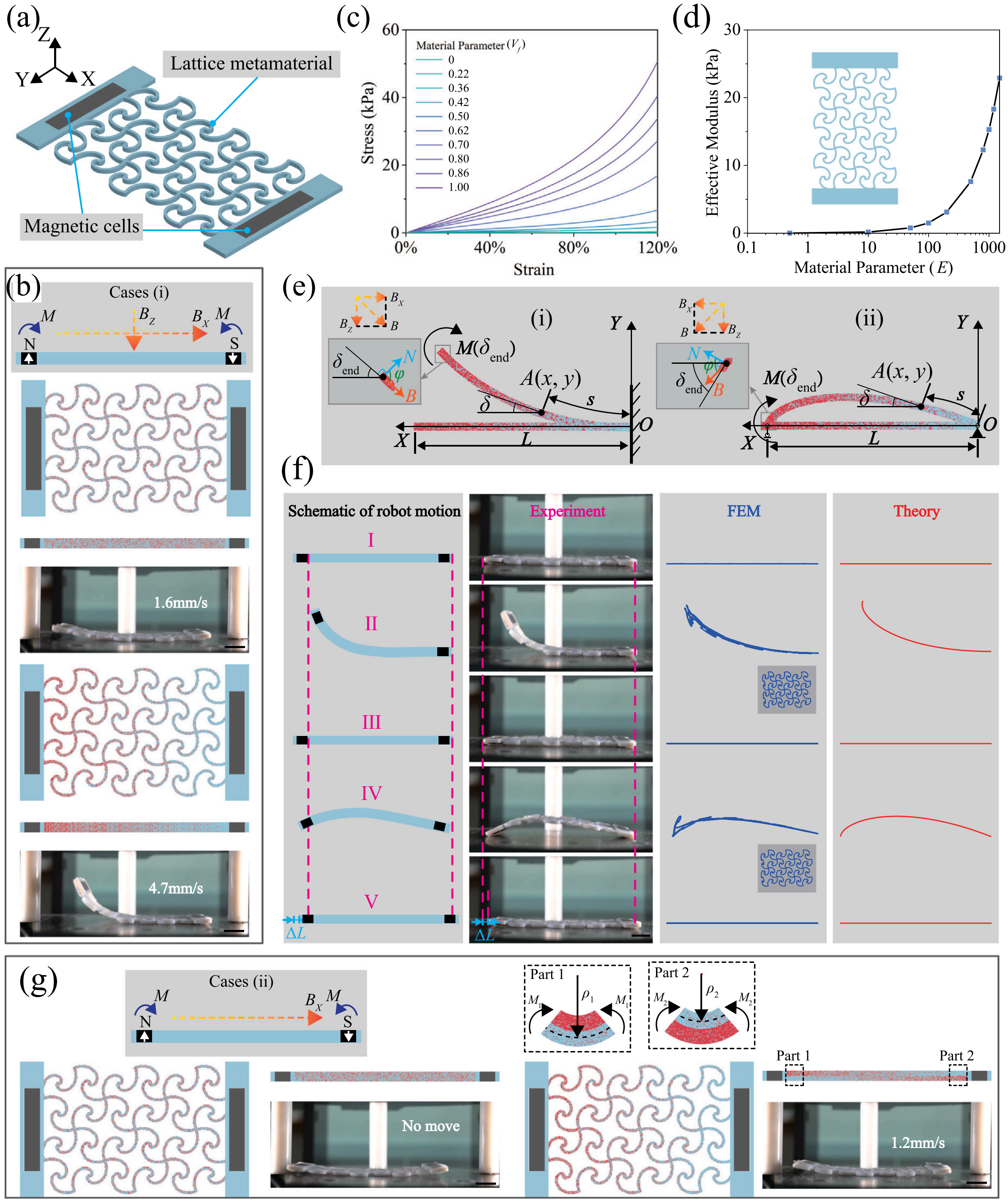

Fig. 6. Magnetic voxel lattice soft robot. (a) The magnetic soft robot consists of a 3D voxel printed rectangular lattice metamaterial and two magnetic cells. (b) Case (i). Under a combined magnetic field B_X (sinusoidal) and B_Z (constant), the soft robot with homogenized material moves at a speed of 1.6 mm/s, while the soft robot with lateral-graded material distribution moves at 4.7 mm/s. (c) The theoretical stress–strain curves of voxel lattice material with different material parameters (V_f). (d) shows the corresponding effective modulus. (e) An analytical model to for crawling motion of the magnetic soft robot. (f) The comparison between theoretical bending deformations with the FEM simulated and experimental results of the soft robot with the lateral-graded material distribution. (g) Case (ii). Under a sinusoidal magnetic field B_X, the magnetic soft robot with homogenized material does not move, while the soft robot with biaxial-graded material moves towards the right direction at 1.2 mm/s. All scale bars are 10 mm.

The deformed shape of the beam can be constructed by solving the differential equation Eq. (16) with boundary condition Eq. (19) and load requirement Eq. (18). Note that the direction of B changes due to the change of B_X direction.

As shown in Fig. 6(f), the developed beam models were used to predict the motion of the soft robot with the lateral-graded material distribution. The theoretical bending deformations agreed with the FEM simulated and experimental results, indicating that the non-homogeneous material distribution breaks the symmetry and leads to directional locomotion. The quasi-static analytical model allowed guidance for designing magnetic voxel lattice soft robots. We should note that the theoretical model for the magnetic soft robot is simplified due to the complex structures and material distributions, and unable to predict the behaviors of the bilateral-graded soft robots.

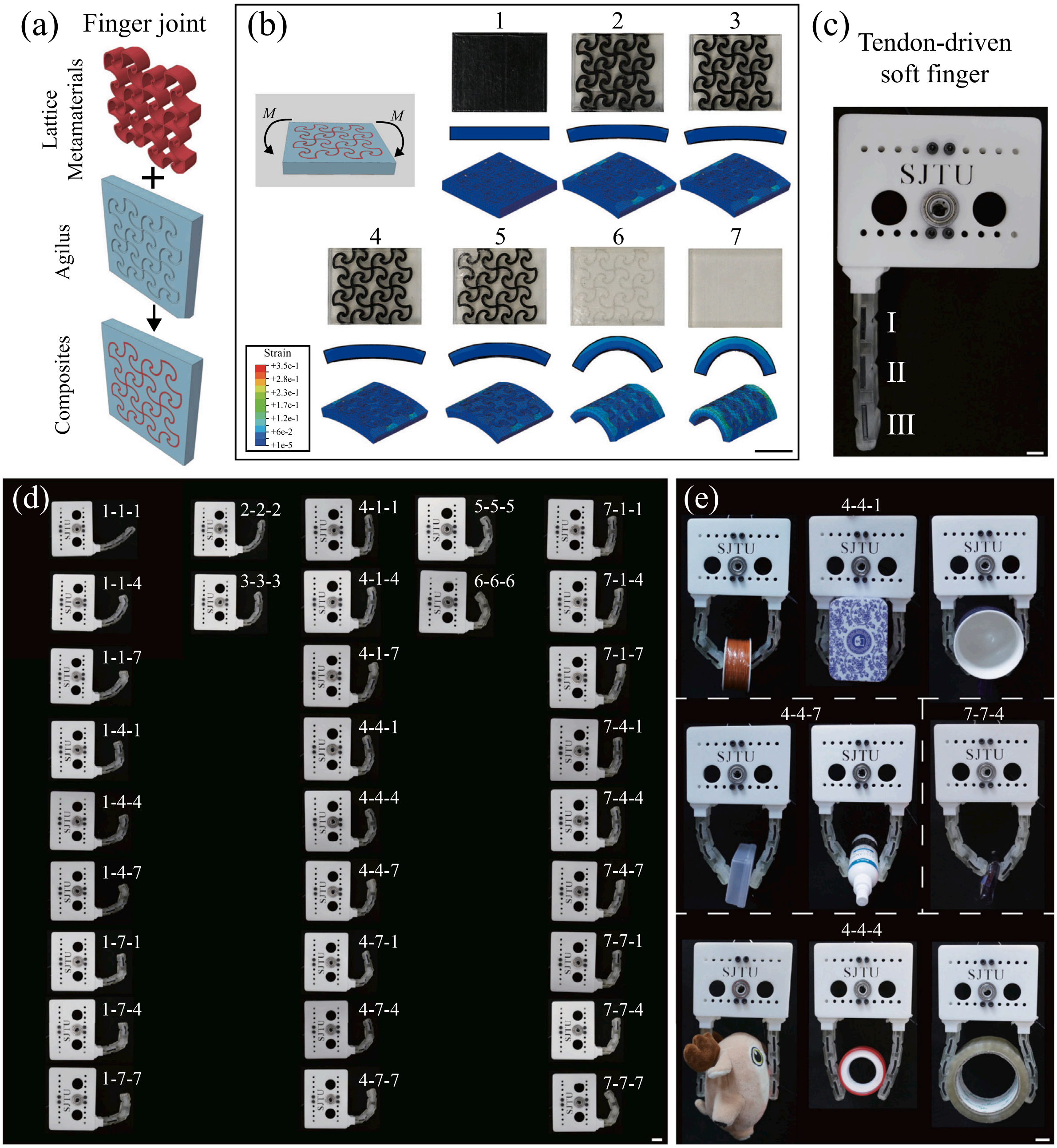

Fig. 7. Tendon-driven soft fingers with three variable stiffness joints. (a) Schematic diagram of the finger joint. (b) Seven different stiffness finger joints and the corresponding FEM simulated deformation under bending moment M (1.5 N · mm). 1: Vero; 2-6: Composites consisted of lattice metamaterials and Agilus; 7: Agilus. (c) The undeformed shape of soft fingers with three joints (I, II and III). (d) The deformed shapes show programmable configurations using different stiffness finger joints. (e) Grasping with controllable curvatures via assembled modular fingers. All scale bars are 10 mm.

In case (ii), the lattice soft robot with homogenized material bent and curled symmetrically with no horizontal locomotion. In contrast, the lattice with biaxial-graded material distribution showed a crawling motion toward the X direction with a speed of 1.2 mm/s. The non-homogeneous material distribution shifted the location of the neutral axis of lattices, thus the bending stiffness of part 1 was lower than part 2 which broke the symmetry and led to directional locomotion. The voxel-level design strategies enable the programmable locomotion of soft robots.

5.4. Voxel soft grippers

Developing a soft gripper with controllable curvatures is essential for highly adaptable robotic hands with applications in industrial and medical areas. The voxel printing method enabled the design of soft grippers with controllable curvatures.

As shown in Fig. 7, we designed assembled modular finger. Seven joints are designed. Joint 1 was made by pure Vero. Other joints consisted of voxel-printed lattice metamaterials (Vero) and soft matrix (Agilus) (Fig. 7(a)). The volume fractions of the embedded lattice were 1, 0.8, 0.62, 0.36, 0.02 and 0 for joints 2 to 7. By varying the volume fractions, the finger joints showed various stiffness. Fig. 7(b) depicts the FEM simulated bending shapes of 7 joints under moment M (1.5 N · mm). Tie constraints were used between the surface of the lattice metamaterials and the matrix. The finger joints show programmable bending stiffness and can be applied in soft grippers to realize controllable curvatures.

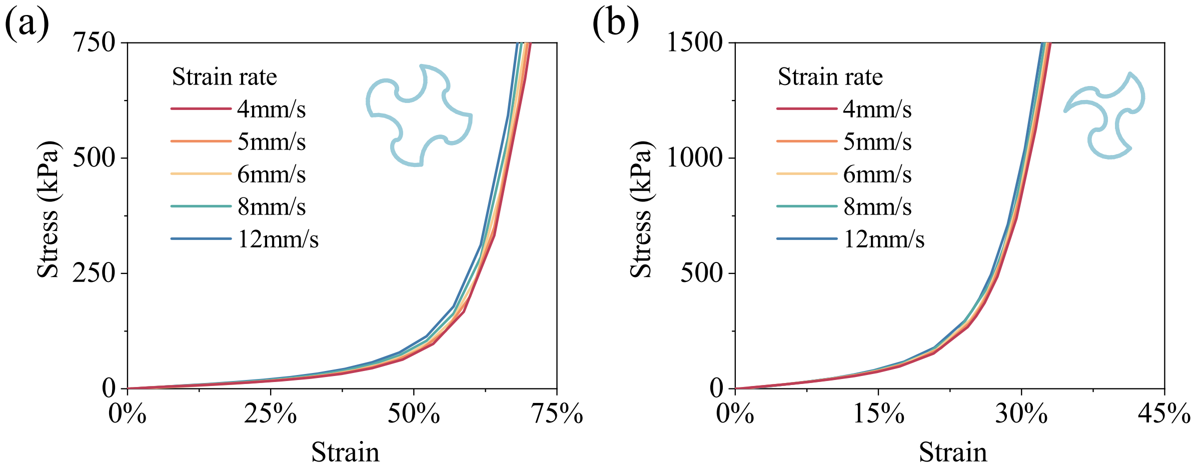

Fig. 8. The effect of strain rate on stress–strain curves of (a) rectangular and (b) triangular voxel lattice metamaterial.

The soft gripper was assembled by a soft matrix and three joints (Fig. 7(c)). Fig. 7(d) shows the configurations of the modular fingers with different combinations of joints. All the fingers were pulled by the same length 60 mm. Different joint combinations led to different finger configurations. The fingers displayed a nearly constant curvature configuration if the same joints were used. Controllable curvatures can be realized by using different joint combinations. For example, if a 1-4-1 type was used, the middle joint was softer than the other two, resulting in a nearly two-segment configuration with a large fold at the middle. Similarly, 1-7-1 formed a nearly horizontal vertical configuration. In contrast, the finger was almost vertical if the first joint was soft, as shown by 7-4-1 and 7-4-4. The soft fingers also exhibited self-adapting properties. Fig. 7(e) shows the obtained grasps using two modular fingers to grasp various objects with different shapes, weights and dimensions. The stable grasp in different scenarios confirms the grasping ability and curvature controllability of the gripper.

6. Discussions

6.1. Inverse design process

The inverse design process was enabled by machine learning (ML) and evolutionary algorithm (EA). For stress–strain matching, a series of voxel lattice metamaterials were constructed by tuning the geometric (n) and material parameters (E) of microstructures I-III first. The theoretical model was then used to evaluate the stress–strain responses of lattice metamaterials to form the database for ML. Next, an ANN-based ML model was established by learning the database. The input was the design parameters, and the output was the corresponding stress–strain curve. The ML model was served as a surrogate model for fast and precise prediction of stress–strain curves. Last, the ML model was combined with the EA to obtain the optimal design with the target stress–strain curve. The EA involved the initial generation establishment, selection, crossover, and mutation. We demonstrated that the rationally designed triangular metamaterial can simultaneously mimic the J-shaped stress–strain curves and negative Poisson's ratio of the cat's skin. In our previous study [51], a python-assisted FEM model was used to form the database for training the machine learning model in the optimization process. In this work, the database for the inverse design of the stress–strain curve was generated by the developed theoretical model. Benefiting from the low computation costs of the theoretical model, the time consumed in forming the database using the theoretical model is lower than that of using the FEM model.

The developed ML-EA approach was further used for shape-matching designs. Three subregions were applied with individually designed microstructures. The lateral profiles of a porcelain vase can be accurately reproduced. The python-assisted FEM model was utilized to form the database as boundary conditions between subregions are complex [51].

6.2. Viscoelasticity

We used the linear elasticity constitutive model. The three-dimensional Timoshenko beam was used. Linear elasticity was used because the local strain of the material was generally less than 5% when the overall strain of the lattice structure exceeds 100% [36,53]. Noted that Vero and Agilus are both shape memory polymers with viscoelasticity. Viscoelasticity also affects their mechanical behaviors. We had studied the effect of viscoelasticity and strain rate based on the multi-branch constitutive model developed in our previous study [54]. Based on the model, we analyzed the effect of strain rate on stress–strain curves of voxel lattice metamaterial at room temperature (20 °C). As shown in Fig. 8, the tangent modulus of rectangular and triangular lattice metamaterial slightly increased as the strain rate increased. For instance, the stress increased from 218.4 kPa to 239.4 kPa at $\varepsilon = 30\%$ as the strain rate applied on triangular lattice metamaterial increased from 4 mm/s to 12 mm/s.

6.3. FEM simulations

The mesh convergence study for the FEM models was conducted for both the rectangular and triangular voxel lattice metamaterials. The FEM simulated stress at $\varepsilon = 60\%$ for the rectangular lattice and $\varepsilon = 20\%$ for the triangular lattice with different mesh sizes are shown in Fig. S12(a) and (b), respectively. By progressively decreasing the mesh size, the number of elements increases from 5000 to 80000. The results showed that the number of elements should be larger than 15000 to ensure computational accuracy. Therefore, 20000 elements are adopted in the FEM simulations.

We used the B32H (3D Timoshenko beam) elements in FEM due to the following reasons.

(1) The use of B32H element (considering both shear and out-of-plane deformation) is a more accurate representation of the experimental conditions, as both shear and out-of-plane deformation may exist in the experiments. Its applications in lattice structure have been verified by previous studies [36,38,55].

(2) The main difference between Euler–Bernoulli and Timoshenko beams is the shear effect. The FEM results using B32H show that the shear strain and stress are small (Fig. S13(a)). Also, the Euler–Bernoulli beam model is a good approximation to the Timoshenko beam model when $EI/K_sL_s^2AG \ll 1$ [56], where E is the elastic modulus; I is the second moment inertia; K_s is Timoshenko shear coefficient, G is the shear modulus; A is the area of cross-section; L_s is the length

of the beam. In this work, $EI/K_sL_s^2AG =\sim 10^{-3} \ll 1$. Therefore, the difference between Euler–Bernoulli and Timoshenko beams can be neglected.

(3) The FEM simulation using 2D and 3D Euler–Bernoulli beam elements (B23H and B33H) do not converge for complex microstructures.

The FEM simulation takes into account the out-of-plane deformation. The out-of-plane deformation exists in experiments, although it is small and neglected in the theoretical model. The FEM results with or without out-of-plane deformation are almost identical. As can be seen from Fig.S13(b), the FEM simulated stress–strain curve of a typical lattice metamaterial using 2D (B22H) or 3D (B32H) Timoshenko beams almost coincide. The out-of-plane deformation could be large when under a large deformation or specific structural designs are involved, as studied in previous work [8,57].

6.4. *3D voxel structures*

The voxel printed method provides an opportunity to design 3D voxel lattice metamaterials. Both material and geometric parameters can be used to design multifunctionalities. In addition, the straight beams in a 3D lattice can be replaced by curled microstructures to improve the stretchability in multiple directions. The potential applications range from 3D flexible electronics [58], energy absorption [59], structured fabrics [32] to medical stents [60]. However, both fabrication and design are current challenges. Printing 3D voxel structures may need a large amount of supporting material, which is difficult to be removed and can easily lead to structural failures. Developing theoretical model for 3D voxel structures is also difficult due to the complex structure and material distribution. The wide material and structural design spaces further hinder inverse design. Combining high-resolution and support-free voxel 3D printing technologies, mathematics-based modeling methods, and topological optimization may pave the way for designing 3D voxel lattice metamaterials.

7. Conclusion

3D voxel printing allows for voxel-level material distributions, while lattice metamaterials can provide multifunctions by structural design. This work aims to develop a design framework for voxel-printed lattice structures and explore their wide design spaces, which have not been studied before based on our best knowledge. The theoretical model is developed based on previous work, which focused mainly on structural design and neglected voxel-level material distributions. By combining the modulus and geometry changes (modified modulus/cross-section term) caused by the voxel printing and the previously developed theoretical model of lattice structures, the theoretical model is established for the voxel lattice and enables the design using both geometric and material parameters. The developed theoretical model shows three innovations: (i) $E(\alpha)$ is applied to characterize the microstructures with gradient voxel distributions; (ii) $I(\alpha)$ is used to account for varying cross-sections; (iii) lattice metamaterials whose representative unit consisting of different microstructures can be modeled, while the microstructures in a unit are the generally same in previous work [61].

In summary, we develop a combined theoretical, FEM and experimental design framework for 3D voxel printed lattice metamaterials. We extend a previously developed model for lattice metamaterials by considering the voxel-level material distributions and various microstructures. A python-assisted FEM model is developed for the voxel structures. We develop a parametric algorithm to generate the voxel matrix for manufacturing. Experiments are conducted to validate the theoretical and FEM models. The framework is used to design programmable mechanical behaviors, such as Poisson's ratio and stretchability, by tuning the geometric and material parameters. Multifunctional designs of bionic stiffness and Poisson's ratio simultaneously reproduction and shape matching are demonstrated. We also present a magnetic voxel lattice soft robot with directional locomotion. This work paves the way for designing and manufacturing 3D voxel printed lattice metamaterial with multifunctionality.

CRediT authorship contribution statement

Le Dong: Writing – review & editing, Writing – original draft, Visualization, Validation, Software, Resources, Methodology, Investigation, Formal analysis, Data curation. **Jinqiang Wang:** Writing – original draft, Visualization, Validation, Methodology, Investigation. **Dong Wang:** Writing – review & editing, Writing – original draft, Visualization, Validation, Software, Resources, Project administration, Methodology, Investigation, Funding acquisition, Formal analysis, Data curation, Conceptualization.

Declaration of competing interest

The authors declare that they have no known competing financial interests or personal relationships that could have appeared to influence the work reported in this paper.

Data availability

Data will be made available on request

Acknowledgments

D.W. acknowledges support from Supported by the National Key Research and Development Program of China (No. 2022YFB4700900), the National Natural Science Foundation of China (Grant No. 52275025), the Interdisciplinary Program of Shanghai Jiao Tong University, China (Grant No. YG2021QN105) and the State Key Laboratory of Mechanical System and Vibration, China (Grant No. MSVZD202212).

Appendix A. Supplementary data

Supplementary material related to this article can be found online at https://doi.org/10.1016/j.addma.2023.103532.

References

[1] T. Zhang, Z. Huang, T. Yang, H. Kong, J. Luan, A. Wang, D. Wang, W. Kuo, Y. Wang, C.-T. Liu, In situ design of advanced titanium alloy with concentration modulations by additive manufacturing, Science 374 (6566) (2021) 478–482.

[2] D. Gu, X. Shi, R. Poprawe, D.L. Bourell, R. Setchi, J. Zhu, Material-structure-performance integrated laser-metal additive manufacturing, Science 372 (6545) (2021) eabg1487.

[3] J. Ren, Y. Zhang, D. Zhao, Y. Chen, S. Guan, Y. Liu, L. Liu, S. Peng, F. Kong, J.D. Poplawsky, et al., Strong yet ductile nanolamellar high-entropy alloys by additive manufacturing, Nature 608 (7921) (2022) 62–68.

[4] D. Gräfe, A. Wickberg, M.M. Zieger, M. Wegener, E. Blasco, C. Barner-Kowollik, Adding chemically selective subtraction to multi-material 3D additive manufacturing, Nature Commun. 9 (1) (2018) 1–6.

[5] D. Kokkinis, M. Schaffner, A.R. Studart, Multimaterial magnetically assisted 3D printing of composite materials, Nature Commun. 6 (1) (2015) 1–10.

[6] Y.-F. Zhang, N. Zhang, H. Hingorani, N. Ding, D. Wang, C. Yuan, B. Zhang, G. Gu, Q. Ge, Fast-response, stiffness-tunable soft actuator by hybrid multimaterial 3D printing, Adv. Funct. Mater. 29 (15) (2019) 1806698.

[7] N.W. Bartlett, M.T. Tolley, J.T. Overvelde, J.C. Weaver, B. Mosadegh, K. Bertoldi, G.M. Whitesides, R.J. Wood, A 3D-printed, functionally graded soft robot powered by combustion, Science 349 (6244) (2015) 161–165.

[8] J.W. Boley, W.M. Van Rees, C. Lissandrello, M.N. Horenstein, R.L. Truby, A. Kotikian, J.A. Lewis, L. Mahadevan, Shape-shifting structured lattices via multimaterial 4D printing, Proc. Natl. Acad. Sci. 116 (42) (2019) 20856–20862.

[9] T. van Manen, S. Janbaz, A.A. Zadpoor, Programming the shape-shifting of flat soft matter, Mater. Today 21 (2) (2018) 144–163.

[10] M.O.F. Emon, F. Alkadi, D.G. Philip, D.-H. Kim, K.-C. Lee, J.-W. Choi, Multi-material 3D printing of a soft pressure sensor, Addit. Manuf. 28 (2019) 629–638.

[11] K. Che, C. Yuan, H.J. Qi, J. Meaud, Viscoelastic multistable architected materials with temperature-dependent snapping sequence, Soft Matter 14 (13) (2018) 2492–2499.

[12] K. Che, M. Rouleau, J. Meaud, Temperature-tunable time-dependent snapping of viscoelastic metastructures with snap-through instabilities, Extreme Mech. Lett. 32 (2019) 100528.

[13] M.A. Skylar-Scott, J. Mueller, C.W. Visser, J.A. Lewis, Voxelated soft matter via multimaterial multinozzle 3D printing, Nature 575 (7782) (2019) 330–335.

[14] G.H. Loh, E. Pei, D. Harrison, M.D. Monzón, An overview of functionally graded additive manufacturing, Addit. Manuf. 23 (2018) 34–44.

[15] J. Chen, L. Zhao, K. Zhou, Multi jet fusion 3D voxel printing of conductive elastomers, Adv. Mater. (2022) 2205909.

[16] I.F. Ituarte, N. Boddeti, V. Hassani, M.L. Dunn, D.W. Rosen, Design and additive manufacture of functionally graded structures based on digital materials, Addit. Manuf. 30 (2019) 100839.

[17] C. Bader, D. Kolb, J.C. Weaver, S. Sharma, A. Hosny, J. Costa, N. Oxman, Making data matter: Voxel printing for the digital fabrication of data across scales and domains, Sci. Adv. 4 (5) (2018) eaas8652.

[18] E. Sachyani Keneth, A. Kamyshny, M. Totaro, L. Beccai, S. Magdassi, 3D printing materials for soft robotics, Adv. Mater. 33 (19) (2021) 2003387.

[19] E.B. Joyee, A. Szmelter, D. Eddington, Y. Pan, 3D printed biomimetic soft robot with multimodal locomotion and multifunctionality, Soft Robot. 9 (1) (2022) 1–13.

[20] X. Li, L. Lu, J. Li, X. Zhang, H. Gao, Mechanical properties and deformation mechanisms of gradient nanostructured metals and alloys, Nat. Rev. Mater. 5 (9) (2020) 706–723.

[21] L. Ren, Z. Wang, L. Ren, Z. Han, Q. Liu, Z. Song, Graded biological materials and additive manufacturing technologies for producing bioinspired graded materials: An overview, Composites B (2022) 110086.

[22] Z. Liu, M.A. Meyers, Z. Zhang, R.O. Ritchie, Functional gradients and heterogeneities in biological materials: Design principles, functions, and bioinspired applications, Prog. Mater. Sci. 88 (2017) 467–498.

[23] F. Pati, J. Jang, D.-H. Ha, S. Won Kim, J.-W. Rhie, J.-H. Shim, D.-H. Kim, D.-W. Cho, Printing three-dimensional tissue analogues with decellularized extracellular matrix bioink, Nature Commun. 5 (1) (2014) 1–11.

[24] R.O. Hynes, The extracellular matrix: Not just pretty fibrils, Science 326 (5957) (2009) 1216–1219.

[25] S. Ansari, S. Khorshidi, A. Karkhaneh, Engineering of gradient osteochondral tissue: From nature to lab, Acta Biomater. 87 (2019) 41–54.

[26] M.J. Harrington, P. Fratzl, Natural load-bearing protein materials, Prog. Mater. Sci. 120 (2021) 100767.

[27] H. Peisker, J. Michels, S.N. Gorb, Evidence for a material gradient in the adhesive tarsal setae of the ladybird beetle Coccinella septempunctata, Nature Commun. 4 (1) (2013) 1–7.

[28] A.M. Torres, A.A. Trikanad, C.A. Aubin, F.M. Lambers, M. Luna, C.M. Rimnac, P. Zavattieri, C.J. Hernandez, Bone-inspired microarchitectures achieve enhanced fatigue life, Proc. Natl. Acad. Sci. 116 (49) (2019) 24457–24462.

[29] Z. Jia, Y. Yu, S. Hou, L. Wang, Biomimetic architected materials with improved dynamic performance, J. Mech. Phys. Solids 125 (2019) 178–197.

[30] S.H. Siddique, P.J. Hazell, H. Wang, J.P. Escobedo, A.A. Ameri, Lessons from nature: 3D printed bio-inspired porous structures for impact energy absorption–a review, Addit. Manuf. (2022) 103051.

[31] H. Cui, D. Yao, R. Hensleigh, H. Lu, A. Calderon, Z. Xu, S. Davaria, Z. Wang, P. Mercier, P. Tarazaga, et al., Design and printing of proprioceptive three-dimensional architected robotic metamaterials, Science 376 (6599) (2022) 1287–1293.

[32] Y. Wang, L. Li, D. Hofmann, J.E. Andrade, C. Daraio, Structured fabrics with tunable mechanical properties, Nature 596 (7871) (2021) 238–243.

[33] M.C. Fernandes, J. Aizenberg, J.C. Weaver, K. Bertoldi, Mechanically robust lattices inspired by deep-sea glass sponges, Nature Mater. 20 (2) (2021) 237–241.

[34] K. Bertoldi, V. Vitelli, J. Christensen, M. Van Hecke, Flexible mechanical metamaterials, Nat. Rev. Mater. 2 (11) (2017) 1–11.

[35] Y. Ling, W. Pang, J. Liu, M. Page, Y. Xu, G. Zhao, D. Stalla, J. Xie, Y. Zhang, Z. Yan, Bioinspired elastomer composites with programmed mechanical and electrical anisotropies, Nature Commun. 13 (1) (2022) 1–11.

[36] Q. Ma, H. Cheng, K.-I. Jang, H. Luan, K.-C. Hwang, J.A. Rogers, Y. Huang, Y. Zhang, A nonlinear mechanics model of bio-inspired hierarchical lattice materials consisting of horseshoe microstructures, J. Mech. Phys. Solids 90 (2016) 179–202.

[37] J. Zhao, F. Zhang, X. Guo, Y. Huang, Y. Zhang, H. Wang, Torsional deformation dominated buckling of serpentine structures to form three-dimensional architectures with ultra-low rigidity, J. Mech. Phys. Solids 155 (2021) 104568.

[38] J. Liu, D. Yan, Y. Zhang, Mechanics of unusual soft network materials with rotatable structural nodes, J. Mech. Phys. Solids 146 (2021) 104210.

[39] Y. Su, S. Wang, Y. Huang, H. Luan, W. Dong, J.A. Fan, Q. Yang, J.A. Rogers, Y. Huang, Elasticity of fractal inspired interconnects, Small 11 (3) (2015) 367–373.

[40] X. Peng, X. Kuang, D.J. Roach, Y. Wang, C.M. Hamel, C. Lu, H.J. Qi, Integrating digital light processing with direct ink writing for hybrid 3D printing of functional structures and devices, Addit. Manuf. 40 (2021) 101911.

[41] C.M. Larson, J.J. Choi, P.A. Gallardo, S.W. Henderson, M.D. Niemack, G. Rajagopalan, R.F. Shepherd, Direct ink writing of silicon carbide for microwave optics, Adv. Eng. Mater. 18 (1) (2016) 39–45.

[42] X. Xin, L. Liu, Y. Liu, J. Leng, 4D printing auxetic metamaterials with tunable, programmable, and reconfigurable mechanical properties, Adv. Funct. Mater. 30 (43) (2020) 2004226.

[43] N.A. Traugutt, D. Mistry, C. Luo, K. Yu, Q. Ge, C.M. Yakacki, Liquid-crystal-elastomer-based dissipative structures by digital light processing 3D printing, Adv. Mater. 32 (28) (2020) 2000797.

[44] J. Mueller, J.A. Lewis, K. Bertoldi, Architected multimaterial lattices with thermally programmable mechanical response, Adv. Funct. Mater. 32 (1) (2022) 2105128.

[45] F. Habib, P. Iovenitti, S. Masood, M. Nikzad, Fabrication of polymeric lattice structures for optimum energy absorption using multi jet fusion technology, Mater. Des. 155 (2018) 86–98.

[46] Q. Ge, Z. Chen, J. Cheng, B. Zhang, Y.-F. Zhang, H. Li, X. He, C. Yuan, J. Liu, S. Magdassi, et al., 3D printing of highly stretchable hydrogel with diverse UV curable polymers, Sci. Adv. 7 (2) (2021) eaba4261.

[47] M. Mirzaali, A. Caracciolo, H. Pahlavani, S. Janbaz, L. Vergani, A. Zadpoor, Multi-material 3D printed mechanical metamaterials: Rational design of elastic properties through spatial distribution of hard and soft phases, Appl. Phys. Lett. 113 (24) (2018) 241903.

[48] B. Deng, A. Zareei, X. Ding, J.C. Weaver, C.H. Rycroft, K. Bertoldi, Inverse design of mechanical metamaterials with target nonlinear response via a neural accelerated evolution strategy, Adv. Mater. 34 (41) (2022) 2206238.

[49] Q. Zeng, S. Duan, Z. Zhao, P. Wang, H. Lei, Inverse design of energy-absorbing metamaterials by topology optimization, Adv. Sci. 10 (4) (2023) 2204977.

[50] C.M. Hamel, D.J. Roach, K.N. Long, F. Demoly, M.L. Dunn, H.J. Qi, Machine-learning based design of active composite structures for 4D printing, Smart Mater. Struct. 28 (6) (2019) 065005.

[51] L. Dong, D. Wang, Optimal design of three-dimensional voxel printed multimaterial lattice metamaterials via machine learning and evolutionary algorithm, Phys. Rev. Applied. 18 (2022) 054050.

[52] D. Veronda, R. Westmann, Mechanical characterization of skin—finite deformations, J. Biomech. 3 (1) (1970) 111–124.

[53] D. Wang, Y. Xiong, B. Zhang, Y.-F. Zhang, D. Rosen, Q. Ge, Design framework for mechanically tunable soft biomaterial composites enhanced by modified horseshoe lattice structures, Soft Matter 16 (6) (2020) 1473–1484.

[54] D. Wang, L. Dong, G. Gu, 3D printed fractal metamaterials with tunable mechanical properties and shape reconfiguration, Adv. Funct. Mater. 33 (1) (2023) 2208849.

[55] J. Liu, Y. Zhang, Soft network materials with isotropic negative Poisson's ratios over large strains, Soft Matter 14 (5) (2018) 693–703.

[56] A.I. Lurie, Theory of Elasticity, Springer Science & Business Media, 2010.

[57] J. Liu, T. Gu, S. Shan, S.H. Kang, J.C. Weaver, K. Bertoldi, Harnessing buckling to design architected materials that exhibit effective negative swelling, Adv. Mater. 28 (31) (2016) 6619–6624.

[58] O. Dadras-Toussi, M. Khorrami, A.S.C. Louis Sam Titus, S. Majd, C. Mohan, M.R. Abidian, Multiphoton lithography of organic semiconductor devices for 3D printing of flexible electronic circuits, biosensors, and bioelectronics, Adv. Mater. 34 (30) (2022) 2200512.

[59] S.C. Han, D.S. Kang, K. Kang, Two nature-mimicking auxetic materials with potential for high energy absorption, Mater. Today 26 (2019) 30–39.

[60] D. Yan, J. Chang, H. Zhang, J. Liu, H. Song, Z. Xue, F. Zhang, Y. Zhang, Soft three-dimensional network materials with rational bio-mimetic designs, Nature Commun. 11 (1) (2020) 1180.

[61] L. Dong, D. Wang, J. Wang, C. Jiang, H. Wang, B. Zhang, M.S. Wu, G. Gu, Modeling and design of periodic polygonal lattices constructed from microstructures with varying curvatures, Phys. Rev. Applied. 17 (4) (2022) 044032.